Highly Efficient Bidirectional Series-Resonant DC/DC Converter Over Wide Range of Battery Voltages

Changkyu Bai, *Student Member, IEEE*, Byeongcheol Han, *Member, IEEE*, Bong-Hwan Kwon, *Member, IEEE*, and Minsung Kim, *Member, IEEE*

***Abstract*—This article introduces a highly efficient bidirectional resonant dc/dc converter over wide range of battery voltages for vehicle-to-grid (V2G) capable electric vehicles (EVs). It operates as a pulsewidth-modulation (PWM) full-bridge series-resonant converter in the forward direction and a half-bridge resonant boost converter in the backward direction. One advantage of the proposed converter is that it has a wide voltage gain range in the backward operation. Also, it requires only six active switches. To achieve high efficiency, SiC MOSFETs are used for two bottom switches in the primary side, because only these switches suffer hard switching turn-OFF in both forward and backward directions. Since it operates with fixed-frequency and with PWM control, the magnetic components and passive filters can be optimally designed with respect to the volume and the loss. Thus, the proposed converter achieves low-cost, high-conversion ratio, and high efficiency over a wide range of battery voltages. Detailed analysis of the converter operation is presented along with the design procedure. A 3.3-kW/400-V prototype of the proposed converter has been built to operate for 250–415 V primary source voltages and tested to demonstrate its circuit design.**

***Index Terms*—Bidirectional converter, fixed frequency, half-bridge resonant-boost converter, high efficiency, minimum number of devices, pulsewidth-modulation (PWM) full-bridge series resonant converter.**

Manuscript received January 5, 2019; revised April 3, 2019; accepted July 28, 2019. Date of publication August 5, 2019; date of current version January 10, 2020. This work was supported in part by the Ministry of Science and ICT (MSIT), South Korea, under ICT Consilience Creative Program (IITP-2019-2011-1-00783) supervised by the Institute for Information & Communications Technology Planning & Evaluation (IITP), and in part by Basic Science Research Program through the National Research Foundation of Korea (NRF) funded by the Ministry of Education (2018R1D1A1B07044999). Recommended for publication by Associate Editor A. Khaligh. *(Corresponding author: Minsung Kim.)*

C. Bai is with the Department of Creative IT Engineering, Pohang University of Science and Technology (POSTECH), Pohang 37673, South Korea (e-mail: bck0325@postech.ac.kr).

B. Han is with Future Energy Electronics Center, Virginia Polytechnic Institute and State University (Virginia Tech), Blacksburg, VA 24061 USA (e-mail: hbychol@vt.edu).

B.-H. Kwon is with the Department of Electrical Engineering, POSTECH, Pohang 37673, South Korea (e-mail: bhkwon@postech.ac.kr).

M. Kim is with the Division of Electronics and Electrical Engineering, Dongguk University, Seoul 04620, South Korea (e-mail: mkim@dongguk.edu).

Color versions of one or more of the figures in this article are available online at http://ieeexplore.ieee.org.

Digital Object Identifier 10.1109/TPEL.2019.2933408

I. Introduction

RECENTLY, electric vehicles (EVs) with vehicle-to-grid (V2G) capability have gained much popularity because they are able to recover excessive energy produced by the renewable energy sources, such as wind power, photovoltaic cells, and thermoelectric systems, thereby reducing energy demand and supply imbalance (see Fig. 1). V2G-capable EV is equipped with a bidirectional dc–dc converter (BDC) that can transfer power to the grid and vice versa. The batteries used for EV usually operate at medium power capacity ($\geq$3.3 kW) and over a wide voltage range (250–415 V). BDC must be able to accommodate medium power capacity and achieve high efficiency over wide range of battery voltages.

Among the bidirectional converters, the dual-active-bridge (DAB) converter is considered as the most attractive one because of its efficiency and power performance, and buck/boost operation capability for bidirectional power transfer [1]–[4]. However, it suffers from high reactive power and high turn-OFF loss when the normalized voltage gain is not close to 1, which significantly degrades power conversion efficiency. Although the reactive power can be reduced by using the improved modulation techniques, such as the extended phase-shift [5], dual phase-shift [6], and triple phase-shift [7] methods, the turn-OFF loss is still high.

To reduce the turn-OFF loss of the DAB converters, one promising solution is to operate the converter in a resonant mode by employing the resonant tank. *LLC* resonant converters [8], [9] feature high efficiency, high power density, and low cost in the forward direction. But it operates as a series-resonant converter whose range of voltage gains is very narrow in the backward direction. To solve this problem, *CLLC*- and *CLLLC*-type resonant converters are proposed [10]–[12], where they have symmetrical characteristics in both power flow directions. Nevertheless, the power conversion efficiency degrades when the battery voltage and the switching frequencies vary over a wide range. Variable dc-link voltage control technique has been proposed to maintain its efficiency under wide input voltage variation in [13]. Variable dc-link voltage would cause a difficulty in designing dc–dc converter and dc–ac converter stages. Also, higher dc-link voltage level leads to the use of a high voltage rating dc-link capacitor, which increases the size and cost of the converter.

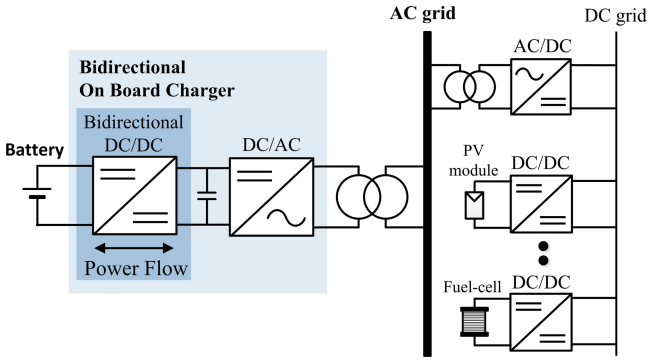

Fig. 1. Configuration of bidirectional on-board charger connected to ac microgrid with multiple energy sources and converters. PV stands for photovoltaic.

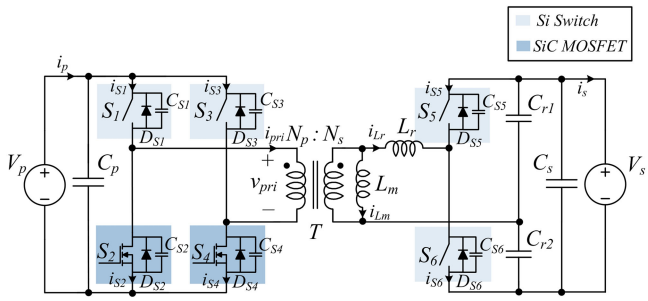

Fig. 2. Circuit diagram of the proposed converter. S_i, D_{Si}, C_{Si} $(i = 1, \ldots, 6)$: equivalent models of the switches. T: transformer with turn ratio $n = N_s/N_p$, where N_p is the number of primary winding turns and N_s is the number of secondary winding turns. C_p and C_s: primary and secondary capacitors. L_m: magnetizing inductor. L_r: resonant inductor. C_{r1} and C_{r2}: resonant capacitors. V_p: primary source voltage. V_s: secondary source voltage. $v_{\rm pri}$: primary side voltage. v_{Cr1} and v_{Cr2}: voltages across C_{r1} and C_{r2}, respectively. i_{Si}: current through the switch S_i $(i = 1, \ldots, 6)$. i_{Lm}: magnetizing current. i_{Lr}: the current that flows through L_r. $i_{\rm pri}$: primary side current. i_p: primary source current. i_s: secondary source current.

To limit switching frequency variations over a wide range of battery voltages, a three-level *LLC* converter with a pulsewidth and amplitude modulation (PWAM) control method is proposed [14]. This converter can achieve soft switching for all switches and wide range of voltage gains with three different control schemes. But a drawback of this converter is that it requires 12 switches. On the other hand, a new bidirectional resonant converter is proposed [15]. By configuring a full-bridge mode and a half-bridge mode operation during each cycle, 0.5-to-1 voltage gain is achieved. However, it does not work when the battery voltage is very low and it still requires a large number of active components on the secondary side. Very recently, a pulsewidth-modulation (PWM) resonant converter is proposed that uses different structures for different modes in [16]. Conventional PWM resonant converter operates in buck-type mode regardless of power flow directions so that it is difficult to maintain discharging operation over entire range of battery voltages. This defect can be overcome by changing the rectifier structure to double the voltage gain. However, when the battery voltage is very low, switching frequency must be adjusted to increase the voltage gain.

In this article, we propose a PWM bidirectional series-resonant converter for a wide range of battery voltages. The proposed converter is equipped with a full-bridge circuit on the primary side and active voltage doubler circuit on the secondary side. In the forward direction, the converter operates as a PWM full-bridge series-resonant converter that achieves high power conversion efficiency by softly switching the primary side switches and reducing the conduction loss. In the backward direction, the converter operates as a half-bridge resonant boost converter that can boost the resonant inductor current by using the bridgeless structure on the primary side. Compared to the conventional bidirectional resonant converters presented in [15] and [16], the proposed converter has a wide voltage gain range from one to infinity in the backward operation. Therefore, the proposed converter achieves high step-up/down capability and high efficiency over wide range of battery voltages. Moreover, this circuit requires only six active switches. SiC MOSFETs are used at the bottom switches on the primary side because only these two switches experience hard switching turn-OFF loss in both forward and backward directions. This aspect can reduce the circuit implementation cost. Furthermore, since it operates with a fixed frequency and with PWM control for all operating conditions, we can design the minimized magnetic components and passive filters dedicated to that frequency. We present detailed circuit operations, steady-state analysis, and design guidelines. We have built the converter prototype operating at 250–415 V battery voltage, 400-V dc-bus voltage, and 3.3-kW rated power, and tested and demonstrated its performance.

This article is organized as follows. The mode analysis of the proposed converter is described in Section II and its steady-state analysis is given in Section III. The design guidelines of the proposed converter are described in Section IV. Experimental results and discussions are presented in Sections V and VI. The conclusions are drawn in Section VII.

II. Topology and System Description

The proposed converter (see Fig. 2) is equipped with a full-bridge circuit on the primary side and an active voltage-doubler rectifier on the secondary side. To analyze steady-state operation of the proposed converter, we made several assumptions.

1) All switches S_1, S_2, S_3, S_4, S_5, and S_6 are ideal except for their body diodes D_{S1}, D_{S2}, D_{S3}, D_{S4}, D_{S5}, and D_{S6}, and output capacitors, C_{S1}, C_{S2}, C_{S3}, C_{S4}, C_{S5}, and C_{S6}.
2) $C_{S1} = C_{S3}, C_{S2} = C_{S4}, C_{S5} = C_{S6}$.
3) T is composed of an ideal transformer with magnetizing inductance and leakage inductance. Note that, L_r is the series connection of the transformer leakage inductance and an external inductance.
4) $C_{r1} = C_{r2}$.
   For subsequent development, we define $C_r = C_{r1} + C_{r2}$; $C_{S13} = C_{S1} = C_{S3}$; $C_{S24} = C_{S2} = C_{S4}$; $C_{S56} = C_{S5} = C_{S6}$.
   The proposed converter operates as a PWM full-bridge series-resonant converter in the forward mode and a half-bridge resonant boost converter in the backward mode, respectively.

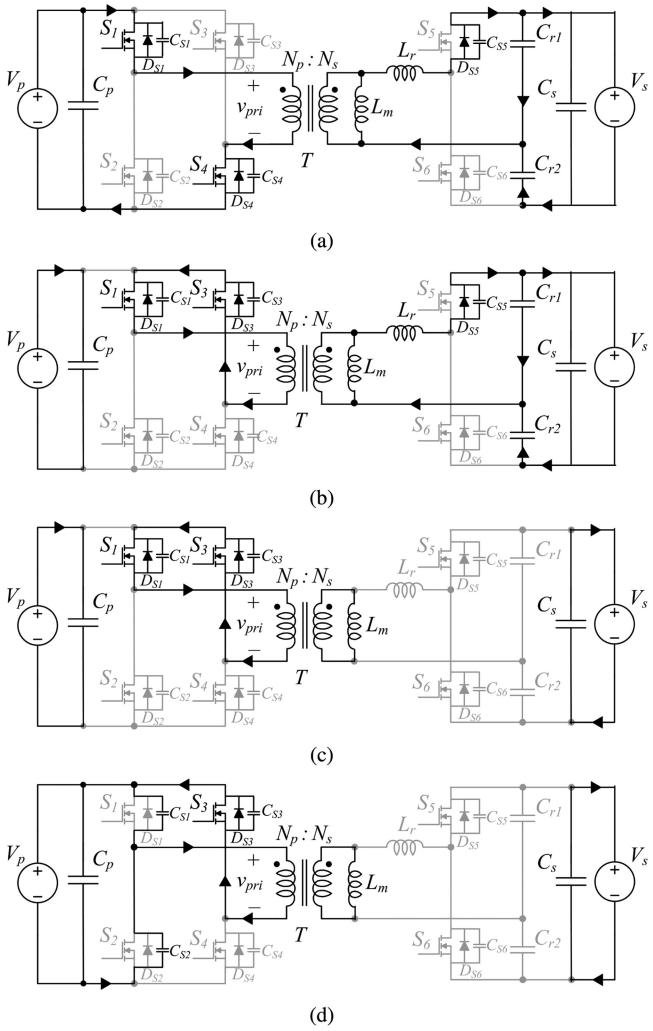

Fig. 3. Equivalent circuits of the proposed converter during the first half-switching period when it operates as a PWM full-bridge series-resonant converter. (a) Mode 1. (b) Mode 2. (c) Mode 3. (d) Mode 4.

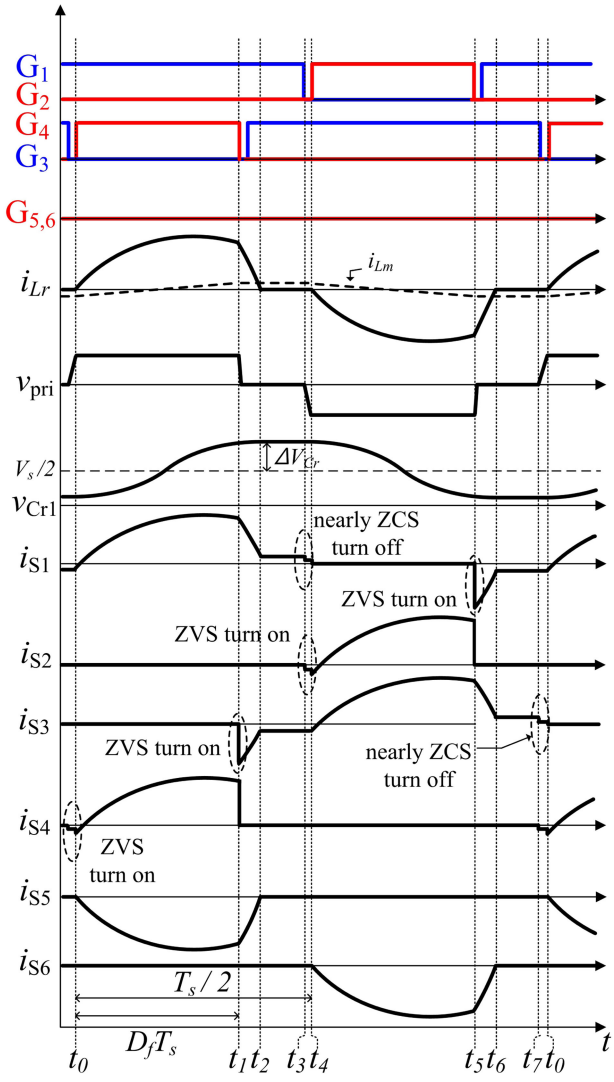

Fig. 4. Waveforms of the proposed converter when it operates as a PWM full-bridge series-resonant converter.

A. Analysis of PWM Full-Bridge Series-Resonant Converter

In the forward direction, this converter operates as a PWM full-bridge series-resonant converter (see Figs. 3 and 4). The primary side switches S_1–S_4 operate in PWM and are driven with the variable duty ratio D_f. In this mode, the bottom switches S_2 and S_4 are softly turned on under almost all operating conditions; the top switches S_1 and S_3 are turned on at zero voltage and turned off near zero current. In this mode, the secondary side switches S_5 and S_6 are always turned off and the active voltage-doubler circuit works as a simple voltage-doubler circuit. The body diodes of the secondary side switches are turned off with almost zero reverse-recovery currents. The switching loss of the converter then becomes very low and the conversion efficiency increases. The detailed analysis is described for the following four modes in the first half-switching period.

Mode 1 [t_0, t_1]: At time t_0, the voltage across S_4 is zero and the primary side current $i_{\rm pri}$ begins to flow through D_{S4}. S_4 is then turned on with zero-voltage switching (ZVS). During this mode, the secondary side voltage is nV_p and i_{Lr} begins to flow through D_{S5}. In this mode, the state equation of the circuit can be written as

$$L_r \frac{di_{Lr}(t)}{dt} = nV_p - v_{Cr1}(t) \tag{1}$$

$$i_{Lr}(t) = C_{r1}\frac{dv_{Cr1}(t)}{dt} - C_{r2}\frac{dv_{Cr2}(t)}{dt} \tag{2}$$

with $i_{Lr}(t_0) = 0$ and $v_{Cr1}(t_0) = V_s/2 - \Delta V_{Cr}$, where ΔV_{Cr} is the voltage ripple of the resonant capacitor. Since V_s is constant, $i_{Lr}(t)$ can be obtained as

$$i_{Lr}(t) = C_{r1}\frac{dv_{Cr1}(t)}{dt} - C_{r2}\frac{d(V_s - v_{Cr1}(t))}{dt} = C_r\frac{dv_{Cr1}(t)}{dt}. \tag{3}$$

Solving (1) and (3) yields

$$i_{Lr}(t) = \frac{r_1}{Z_r}\sin\left[w_r(t-t_0)\right] \tag{4}$$

$$v_{Cr1}(t) = nV_p - r_1\cos\left[w_r(t-t_0)\right] \tag{5}$$

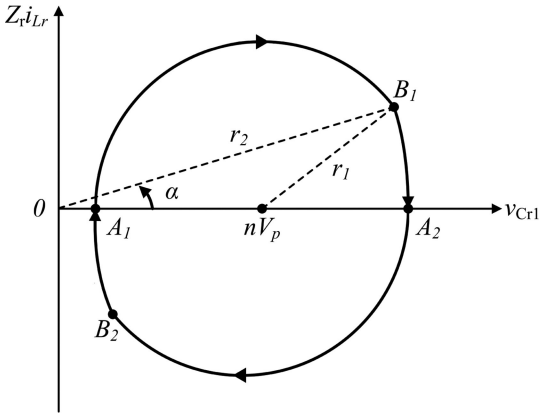

Fig. 5. State-plane trajectory of the proposed converter when it operates as a PWM full-bridge series-resonant converter.

where $r_1 = nV_p - \frac{V_s}{2} + \Delta V_{Cr}$ is the radius of the circular path with the center at $(nV_p, 0)$ as in Fig. 5. The operating point moves along the trajectory curve from A_1 to B_1, as shown in Fig. 5, and the resonant angular frequency w_r and the characteristic impedance Z_r are obtained as

$$w_r = \frac{1}{\sqrt{L_r C_r}}, \quad Z_r = \sqrt{\frac{L_r}{C_r}}. \tag{6}$$

Mode 2 [t_1, t_2]: At time t_1, S_4 is turned off and the current flows through D_{S3}. After the given dead time, S_3 is then turned on with ZVS. Even if $v_{\rm pri}$ drops to 0, D_{S5} is still conducted and $-v_{Cr1}$ is applied to L_r. Thus, i_{Lr} quickly goes to zero. In this mode, the state equation of the circuit can be written as

$$L_r \frac{di_{Lr}(t)}{dt} = -v_{Cr1}(t) \tag{7}$$

$$i_{Lr}(t) = C_r \frac{dv_{Cr1}(t)}{dt} \tag{8}$$

with $i_{Lr}(t_1) = \frac{r_2}{Z_r}\sin\alpha$ and $v_{Cr1}(t_1) = r_2\cos\alpha$, where $\alpha = \cos^{-1}\left(\frac{nV_p}{r_2} - \frac{r_1}{r_2}\cos[w_r(t_1 - t_0)]\right)$. Solving (7) and (8) yields

$$i_{Lr}(t) = \frac{r_2}{Z_r}\sin\left[\alpha - w_r(t - t_1)\right] \tag{9}$$

$$v_{Cr1}(t) = r_2\cos\left[\alpha - w_r(t - t_1)\right] \tag{10}$$

where $r_2 = \frac{V_s}{2} + \Delta V_{Cr}$ is the radius of the circular path with center at (0, 0), as shown in Fig. 5. The operating point moves along the trajectory curve from B_1 to A_2, as shown in Fig. 5.

Mode 3 [t_2, t_3]: At time t_2, i_{Lr} is zero and v_{Cr1} is at its maximum value. During this interval, the current that flows through S_1 and S_3 is the primary side current $i_{\rm pri}$, and it is almost zero. Thus, at time t_3, S_1 gets turned off with nearly zero-current switching (ZCS). At this time, the trajectory path stays at A_2, as shown in Fig. 5.

Mode 4 [t_3, t_4]: At time t_3, S_1 is turned off with almost ZCS, and the converter enters the dead time zone. During this mode, i_{Lm}, which has been continuously charged from time t_0, acts as a current source to the primary side. Primary side current $i_{\rm pri} = ni_{Lm}$ both charges C_{S1} and discharges C_{S2}. When C_{S2} is completely discharged, the voltage across S_2 becomes zero, and $i_{\rm pri}$ flows through D_{S2}. Therefore, at time t_4, S_2 gets turned on with ZVS. The trajectory path still stays at A_2 during this interval.

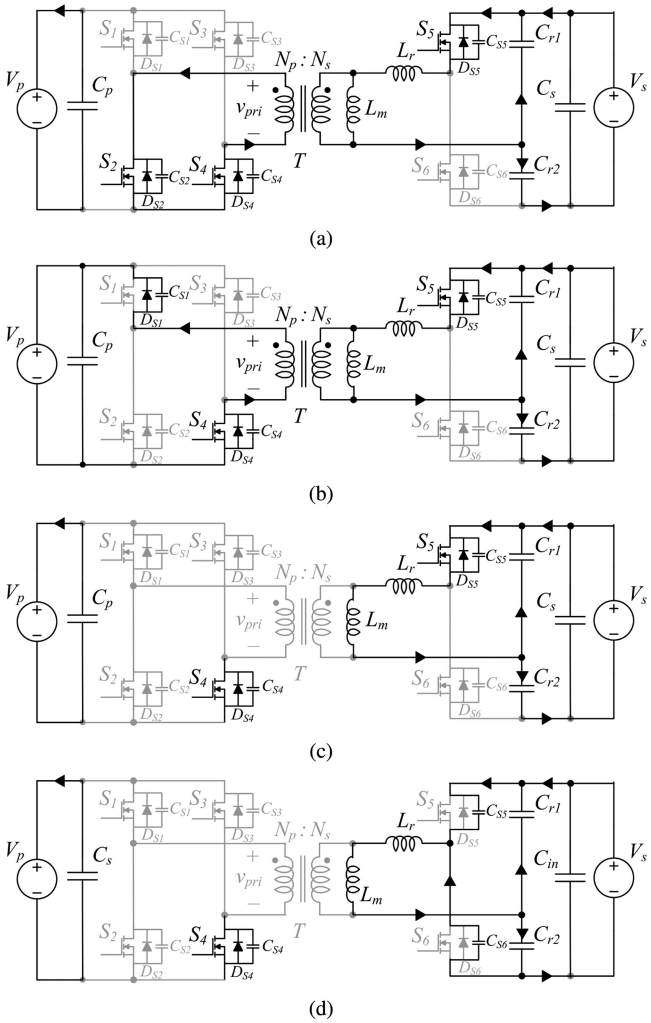

Fig. 6. Equivalent circuits of the proposed converter during the first half-switching period when it operates as a half-bridge resonant boost converter. (a) Mode 1. (b) Mode 2. (c) Mode 3. (d) Mode 4.

During the next first half-switching period, waveforms in the circuit are similar to Modes 1−4.

B. Analysis of Half-Bridge Resonant Boost Converter

In the backward direction, the proposed converter operates as a half-bridge resonant boost converter (see Figs. 6 and 7). Secondary side switches S_5 and S_6 operate with a constant duty ratio 0.5 and in a complementary manner with short dead time. At the same time, S_2 is turned on with the variable duty ratio $0.5 + D_b$ just after turning S_6 ON whereas S_4 is turned on just after turning S_5 ON. S_2 and S_4 help i_{Lr} increase quickly following the sinusoidal waveform. Compared to the conventional converter, the proposed converter is able to increase V_p significantly and, therefore, can be used when the voltage difference between V_p

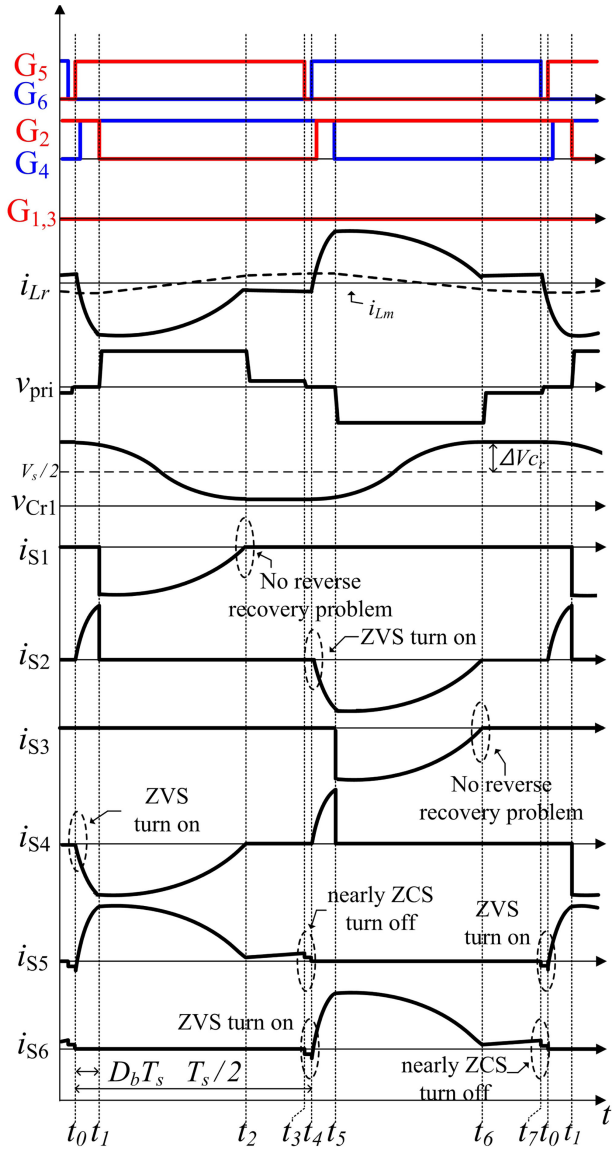

Fig. 7. Waveforms of the proposed converter when it operates as a half-bridge resonant boost converter.

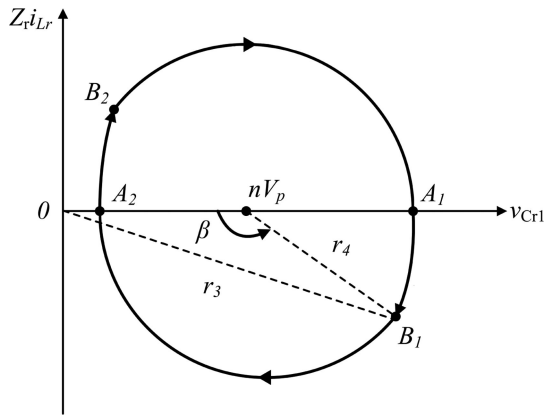

Fig. 8. State-plane trajectory of the proposed converter when it operates as a half-bridge resonant boost converter.

and V_s is very large. The detailed analysis is described for the following four modes in the first half-switching period.

Mode 1 [t_0, t_1]: At time t_0, the voltage across S_5 is zero, and the current begins to flow through D_{S5}. Thus, S_5 is turned on with ZVS. i_{Lr} begins to flow through D_{S4}, and after the given dead time S_4 is then turned on with ZVS. During this interval, the voltage source on the secondary side, the resonant inductor, and the resonant capacitor form an equivalent closed circuit, which boosts the resonant inductor current following the sinusoidal waveform. The state equation corresponding to this equivalent circuit can be written as

$$L_r \frac{di_{Lr}(t)}{dt} = -v_{Cr1}(t) \tag{11}$$

$$i_{Lr}(t) = C_r \frac{dv_{Cr1}(t)}{dt} \tag{12}$$

with $i_{Lr}(t_0) = 0$ and $v_{Cr1}(t_0) = V_s/2 + \Delta V_{Cr}$. Solving (11) and (12) yields

$$i_{Lr}(t) = -\frac{r_3}{Z_r} \sin\left[w_r(t - t_0)\right] \tag{13}$$

$$v_{Cr1}(t) = r_3 \cos\left[w_r(t - t_0)\right] \tag{14}$$

where $r_3 = \frac{V_s}{2} + \Delta V_{Cr}$ is the radius of the circular path with center at (0, 0), as shown in Fig. 8. Here, the operating point moves along the trajectory curve from A_1 to B_1, as shown in Fig. 8.

Mode 2 [t_1, t_2]: At time t_1, S_2 is turned off. The current on the primary side then flows through D_{S1}. During this interval, the primary voltage source, the secondary voltage source, the resonant inductor, and the resonant capacitor form an equivalent closed circuit, and the resonant inductor current goes to zero following the sinusoidal waveform. The state equation corresponding to this equivalent circuit can be written as

$$L_r \frac{di_{Lr}(t)}{dt} = nV_p - v_{Cr1}(t) \tag{15}$$

$$i_{Lr}(t) = C_r \frac{dv_{Cr1}(t)}{dt} \tag{16}$$

with $i_{Lr}(t_1) = -\frac{r_4}{Z_r} \sin\beta$ and $v_{Cr1}(t_1) = nV_p - r_4 \cos\beta$, where $\beta = \cos^{-1}(\frac{nV_p}{r_4} - \frac{r_3}{r_4} \cos[w_r(t_1 - t_0)])$. Solving (15) and (16) yields

$$i_{Lr}(t) = -\frac{r_4}{Z_r} \sin\left[\beta - w_r(t - t_1)\right] \tag{17}$$

$$v_{Cr1}(t) = nV_p - r_4 \cos\left[\beta - w_r(t - t_1)\right] \tag{18}$$

where $r_4 = nV_p - \frac{V_s}{2} + \Delta V_{Cr}$ is the radius of the circular path center at $(nV_p, 0)$, as shown in Fig. 8. The operating point moves along the trajectory curve from B_1 to A_2, as shown in Fig. 8.

Mode 3 [t_2, t_3]: At time t_2, i_{Lr} is zero and v_{Cr1} is at its minimum. During this interval, the current that flows through S_5 is magnetizing current i_{Lm}, and it is almost 0. Thus, at time t_3, the switch S_5 turns OFF with nearly ZCS. Here, the trajectory path stays at point A_2, as shown in Fig. 8.

Mode 4 [t_3, t_4]: At time t_3, S_5 is turned off with almost ZCS and enters the dead time zone. During this time, i_{Lm} appears as a current source to the secondary side, which charges C_{S5}, while discharging C_{S6}. Thus, S_6 is turned on with ZVS. The trajectory path still stays at point A_2 during this interval.

During the next half-switching period, waveforms in the circuit are similar as with Mode 1–4.

III. Steady-State Analysis of the Proposed Converter

A. Voltage Gain of PWM Full-Bridge Series-Resonant Converter

To calculate the voltage gain of the PWM full-bridge series-resonant converter, we first compute the resonant capacitor voltage ripple ΔV_{Cr}. Due to symmetric operation of the voltage-doubler during the steady state, the average value of the resonant inductor current is twice the average secondary source current I_s. Using the fact that $nV_p = r_1 \cos[w_r(t_1 - t_0)] + r_2 \cos\alpha$, which is derived from Fig. 5, we obtain

$$\begin{aligned} I_s = \frac{P_s}{V_s} &= \frac{1}{T_s}\left[\int_{t_0}^{t_1} \frac{r_1}{Z_r}\sin[w_r(\tau - t_0)]d\tau \right. \\ &\quad \left. + \int_{t_1}^{t_2} \frac{r_2}{Z_r}\sin[\alpha - w_r(\tau - t_1)]d\tau\right] \\ &= \frac{1}{T_s Z_r w_r}[r_1 + r_2 - r_1\cos[w_r(t_1 - t_0)] - r_2\cos\alpha] \\ &= \frac{2\Delta V_{Cr}}{T_s Z_r w_r} = \frac{2C_r\Delta V_{Cr}}{T_s} \end{aligned} \tag{19}$$

where P_s is the output power.

Rearranging (19) for ΔV_{Cr} yields

$$\Delta V_{Cr} = \frac{P_s T_s}{2V_s C_r}. \tag{20}$$

As shown in Fig. 5, the circle equations with center $(nV_p, 0)$ and radius r_1, and with center (0, 0) and radius r_2 are, respectively, described as

$$(v_{Cr1}(t) - nV_p)^2 + (Z_r i_{Lr}(t))^2 = r_1^2 \tag{21}$$

$$(v_{Cr1}(t))^2 + (Z_r i_{Lr}(t))^2 = r_2^2. \tag{22}$$

The two circles intersect at point B_1 (see Fig. 5) and at time t_1. Equating (21) and (22) yields

$$\begin{aligned} &(v_{Cr1}(t_1) - nV_p)^2 + (Z_r i_{Lr}(t_1))^2 - r_1^2 \\ &= v_{Cr1}^2(t_1) + (Z_r i_{Lr}(t_1))^2 - r_2^2. \end{aligned} \tag{23}$$

Applying $(t_1 - t_0) = D_f T_s$ to (5), where D_f is the duty ratio of the primary side switches in the forward mode, we can determine $v_{Cr1}(t)$ at t_1 as

$$\begin{aligned} v_{Cr1}(t_1) &= nV_p - r_1\cos[w_r(t_1 - t_0)] \\ &= nV_p - \left(nV_p - \frac{V_s}{2} + \Delta V_{Cr}\right)\cos(w_r D_f T_s). \end{aligned} \tag{24}$$

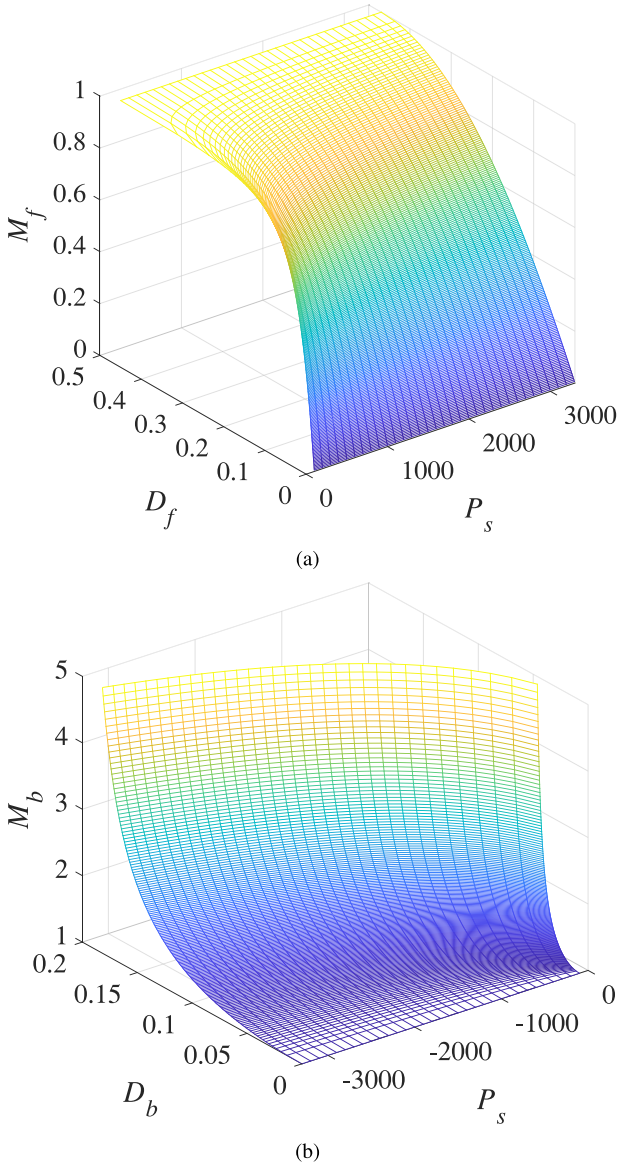

Fig. 9. Voltage gain curves of the proposed converter. (a) M_f. (b) M_b.

Cancelling $(Z_r i_{Lr}(t_1))^2$ terms from both sides of (23), and substituting (24) into (23) yields

$$D_f = \frac{1}{w_r T_s}\cos^{-1}\left(\frac{C_r V_s^2(1 - M_f) + M_f(1 - 2M_f)P_s T_s}{C_r V_s^2(1 - M_f) + M_f P_s T_s}\right) \tag{25}$$

where $M_f = \frac{V_s}{2nV_p}$ is the voltage gain of the PWM full-bridge series-resonant converter.

A three-dimensional (3-D) graph of M_f with respect to D_f and P_s is shown in Fig. 9(a).

B. Voltage Gain of Half-Bridge Resonant Boost Converter

By using the same method as that used to derive the voltage gain of the PWM full-bridge series resonant converter, we

have

$$I_s = \frac{P_s}{V_s} = \frac{1}{T_s}\Big[\int_{t_0}^{t_1} -\frac{r_3}{Z_r}\sin\left[w_r(\tau - t_0)\right]d\tau + \int_{t_1}^{t_2} -\frac{r_4}{Z_r}\sin\left[\beta - w_r(\tau - t_1)\right]d\tau\Big]$$
$$= \frac{1}{T_s Z_r w_r}\left(-r_4 - r_3 + r_4\cos\beta + r_3\cos\left[w_r(t_1 - t_0)\right]\right)$$
$$= -\frac{2\Delta V_{Cr}}{T_s Z_r w_r} = -\frac{2C_r\Delta V_{Cr}}{T_s}. \tag{26}$$

Rearranging (26) for ΔV_{Cr} yields

$$\Delta V_{Cr} = -\frac{P_s T_s}{2V_s C_r}. \tag{27}$$

As shown in Fig. 8, the circle equations with center (0, 0) and radius r_3, and with center $(nV_p, 0)$ and radius r_4 are, respectively, described as

$$(v_{Cr1}(t))^2 + (Z_r i_{Lr}(t))^2 = r_3^2 \tag{28}$$
$$(v_{Cr1}(t) - nV_p)^2 + (Z_r i_{Lr}(t))^2 = r_4^2. \tag{29}$$

The two circles intersect at point B_1 (see Fig. 8) and at time t_1. Equating (28) and (29) yields

$$(v_{Cr1}(t_1))^2 + (Z_r i_{Lr}(t_1))^2 - r_3^2 = (v_{Cr1}(t_1) - nV_p)^2 + (Z_r i_{Lr}(t_1))^2 - r_4^2. \tag{30}$$

Applying $(t_1 - t_0) = D_b T_s$ to (14), where D_b is the duty ratio of the primary side switches in the backward mode, we can determine $v_{Cr1}(t)$ at t_1 as

$$v_{Cr1}(t_1) = r_3\cos\left[w_r(t_1 - t_0)\right] = \left(\frac{V_s}{2} + \Delta V_{Cr}\right)\cos(w_r D_b T_s). \tag{31}$$

Cancelling $(Z_r i_{Lr}(t_1))^2$ terms from both sides of (30) and substituting (31) into (30) yields

$$D_b = \frac{1}{w_r T_s}\cos^{-1}\left(\frac{4n^2 C_r V_p^2 + M_b(2 - M_b)(-P_s)T_s}{M_b^2(-P_s)T_s + 4n^2 C_r V_p^2}\right) \tag{32}$$

where $M_b = \frac{2nV_p}{V_s}$ is the voltage gain of the half-bridge resonant boost converter.

A 3-D graph of M_b with respect to D_b and P_s is shown in Fig. 9(b).

IV. Design Guideline

A. Selection of Transformer Turn Ratio

The turn's ratio of the transformer can be selected from the voltage gain of the proposed converter. It then follows that

$$n \geq \frac{V_s}{2V_{p\_\min}} \tag{33}$$

where $V_{p\_\min}$ is the minimum value of the primary source voltage.

B. Magnetizing Inductance

Because the dead time $t_{\rm dp}$, $t_{\rm ds}$ are very short compared to the switching period T_s, i_{Lm} essentially serves as a constant current source I_{Lm}. In the forward mode, i_{Lm} and i_{Lr} discharge the parasitic output capacitor C_{S2} of S_2 and charge the parasitic output capacitor C_{S1} of S_1 during the dead time as in [17]. To achieve ZVS, i_{Lm} and i_{Lr} must fully discharge C_{S2} of S_2. Thus, ZVS condition in the forward mode is

$$V_p(C_{S13} + C_{S24}) < \int_0^{t_{\rm dp}} |i_{\rm pri}(\tau)|d\tau = n\left(\int_0^{t_{\rm dp}} |i_{Lm}(\tau) + i_{Lr}(\tau)|d\tau\right) = n\left(\int_0^{t_{\rm dp}} (I_{Lm} - i_{Lr}(\tau))d\tau\right) = n\left(I_{Lm}t_{\rm dp} - \int_0^{t_{\rm dp}} \frac{r_1}{Z_r}\sin(w_r\tau)d\tau\right) \simeq n\left(I_{Lm}t_{\rm dp} - \int_0^{t_{\rm dp}} \frac{r_1}{Z_r}w_r\tau d\tau\right) = n\left(I_{Lm}t_{\rm dp} - \frac{r_1 w_r t_{\rm dp}^2}{2Z_r}\right) \tag{34}$$

where $t_{\rm dp}$ is the dead time for the primary side switches. Note that ZVS condition in (34) is checked during the first half-switching period.

Substituting $I_{Lm} = \frac{nV_p D_f T_s}{2L_m}$ into (34) and rearranging it with respect to L_m, we have

$$L_m < \frac{n^2 V_p D_f T_s t_{\rm dp}}{2V_p(C_{S13} + C_{S24}) + \frac{nr_1 w_r t_{\rm dp}^2}{Z_r}}. \tag{35}$$

In the backward mode, i_{Lm} and i_{Lr} discharge C_{S5} and charges C_{S6} during the first half-cycle of the switching period. i_{Lm} and i_{Lr} must fully discharge C_{S6} to achieve ZVS. ZVS condition in the backward mode becomes

$$2V_s C_{S56} < \int_0^{t_{\rm ds}} I_{Lm}d\tau - \int_0^{t_{\rm ds}} \frac{r_3}{Z_r}\sin(w_r\tau)d\tau \simeq I_{Lm}t_{\rm ds} - \frac{r_3 w_r t_{\rm ds}^2}{2Z_r} \tag{36}$$

where $t_{\rm ds}$ is the dead time for the secondary side switches.

Substituting $I_{Lm} = \frac{nV_p D_{bz} T_s + (\frac{V_s}{2} - \Delta V_{Cr})(\frac{1}{2} - D_b - D_{bz})T_s}{2L_m}$ into (36), we have

$$L_m < \frac{\left(nV_p D_{bz} + \left(\frac{V_s}{2} - \Delta V_{Cr}\right)\left(\frac{1}{2} - D_b - D_{bz}\right)\right)T_s t_{\rm ds}}{4V_s C_{S56} + \frac{r_3 w_r t_{\rm ds}^2}{Z_r}}. \tag{37}$$

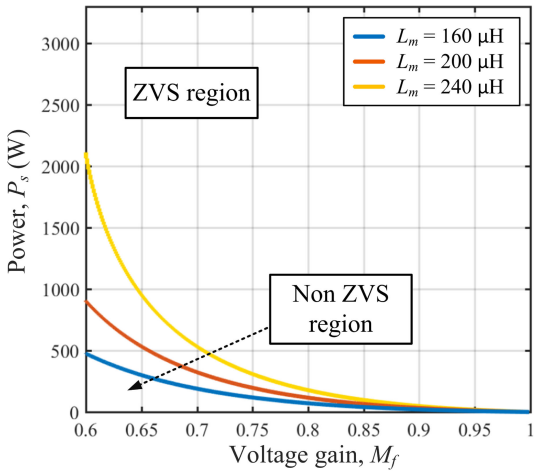

(a)

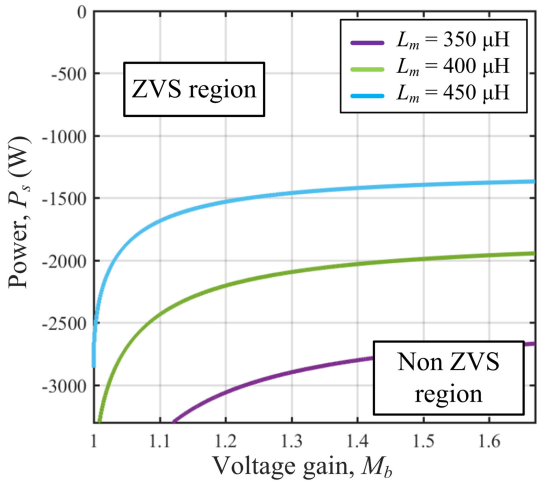

(b)

Fig. 10. ZVS region of the proposed converter with respect to L_m, P_s, and M_f/M_b. (a) Forward operation. (b) Backward operation.

Here, falling duty ratio D_{bz} is

$$D_{bz} = \frac{t_2 - t_1}{T_s} = \frac{\beta}{w_r T_s} = \frac{1}{w_r T_s} \cos^{-1}\left(\frac{nV_p}{r_4} - \frac{r_3}{r_4}\cos(w_r(t_1 - t_0))\right) \quad (38)$$

where

$$\frac{nV_p}{r_4} = \frac{nV_p}{nV_p - \frac{V_s}{2} + \Delta V_{Cr}} = \frac{4n^2V_p^2C_rM_b}{4n^2V_p^2C_rM_b - 4n^2V_p^2C_r + M_b^2(-P_s)T_s} \quad (39)$$

$$\frac{r_3}{r_4} = \frac{\frac{V_s}{2} + \Delta V_{Cr}}{nV_p - \frac{V_s}{2} + \Delta V_{Cr}} = \frac{4n^2V_p^2C_r + M_b^2(-P_s)T_s}{4n^2V_p^2C_rM_b - 4n^2V_p^2C_r + M_b^2(-P_s)T_s} \quad (40)$$

$$\cos(w_r(t_1 - t_0)) = \cos(w_r D_b T_s). \quad (41)$$

TABLE I
PARAMETERS AND COMPONENTS OF THE PROTOTYPE

Parameters	Symbols	Value
Primary source voltage range	V_p	250–415 V
Secondary source voltage	V_s	400 V
Output power	P_s	3.3 kW
Switching frequency	f_s	50 kHz
Resonant frequency	f_r	53.1 kHz
Transformer turns ratio	N_p:N_s	16:13
Magnetizing inductance	L_m	207 μH
Resonant inductance	L_r	14.89 μH
Resonant capacitance	C_{r1}, C_{r2}	0.3 μF
Primary capacitance	C_p	20 μF
Secondary capacitance	C_s	20 μF
Dead time	t_{dp}, t_{ds}	150 ns
Components	**Symbols**	**Part number**
Primary-side top switches	S_1, S_3	IKP40N65H5 (×2)
Primary-side bottom switches	S_2, S_4	UJC06505K
Secondary-side switches	S_5, S_6	IKP40N65H5 (×2)
Transformer core	T	PQ5050

Rearranging (38) yields

$$D_{bz} = \frac{1}{w_r T_s} \cos^{-1}\left(\frac{4n^2V_p^2C_r(M_b - 1) - M_b(2 - M_b)(-P_s)T_s}{4n^2V_p^2C_r(M_b - 1) + M_b^2(-P_s)T_s}\right). \quad (42)$$

Substituting (25), (32), and (42) into (35) and (37), we can present the ZVS region of the switches according to the value of L_m, P_s, and M_f/M_b, as shown in Fig. 10. Larger L_m reduces the ZVS region of the proposed converter. However, smaller L_m generates high peak in i_{Lm} and disturbs ZCS. We selected appropriate value of L_m, which has acceptable ZVS region and generates low peak in i_{Lm}.

C. Resonant Inductance and Resonant Capacitance

To guarantee proper operation of the converter, the voltage across the resonant capacitor must be lower than half of the secondary source voltage for all operating conditions, i.e., $\Delta V_{Cr} \le V_s/2$. From this equation, we have

$$C_r \ge \frac{|P_s|T_s}{V_s^2}. \quad (43)$$

Larger P_s increases the capacitor voltage fluctuation, so the capacitor value should be large enough to satisfy (43). Using (6) and (43), we have

$$L_r \le \frac{V_s^2}{w_r^2|P_s|T_s}. \quad (44)$$

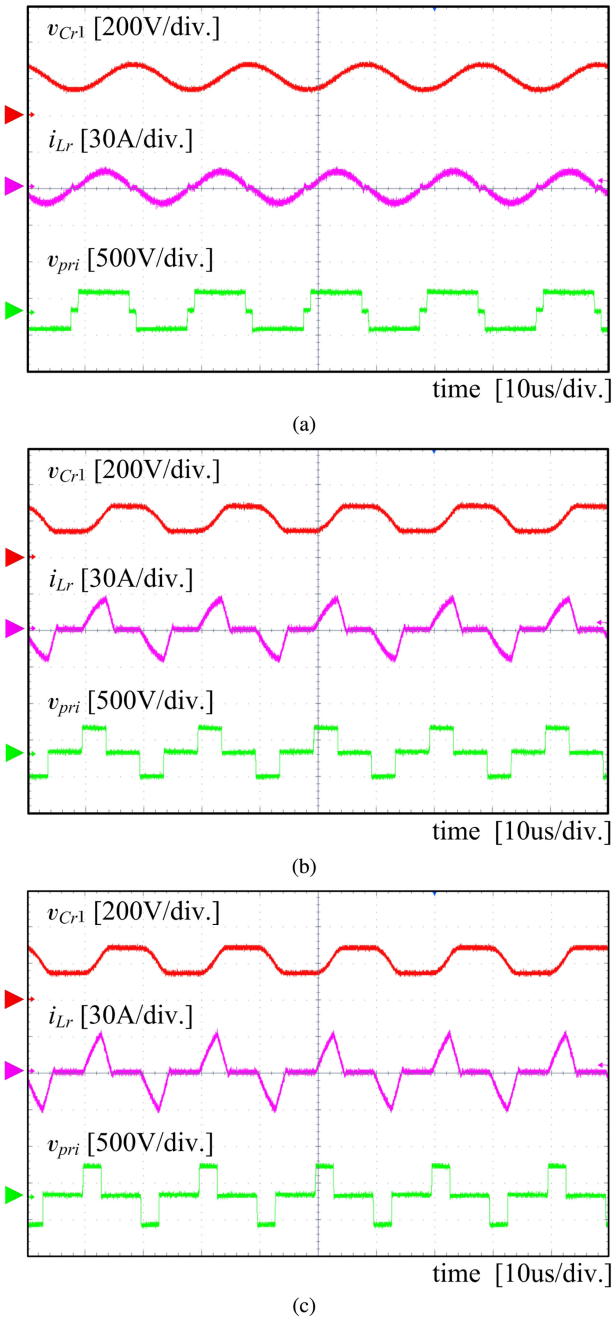

Fig. 11. Experimental waveforms of the proposed converter under half load when it operates as a full-bridge series-resonant converter. (a) $V_p = 250$ V. (b) $V_p = 330$ V. (c) $V_p = 415$ V.

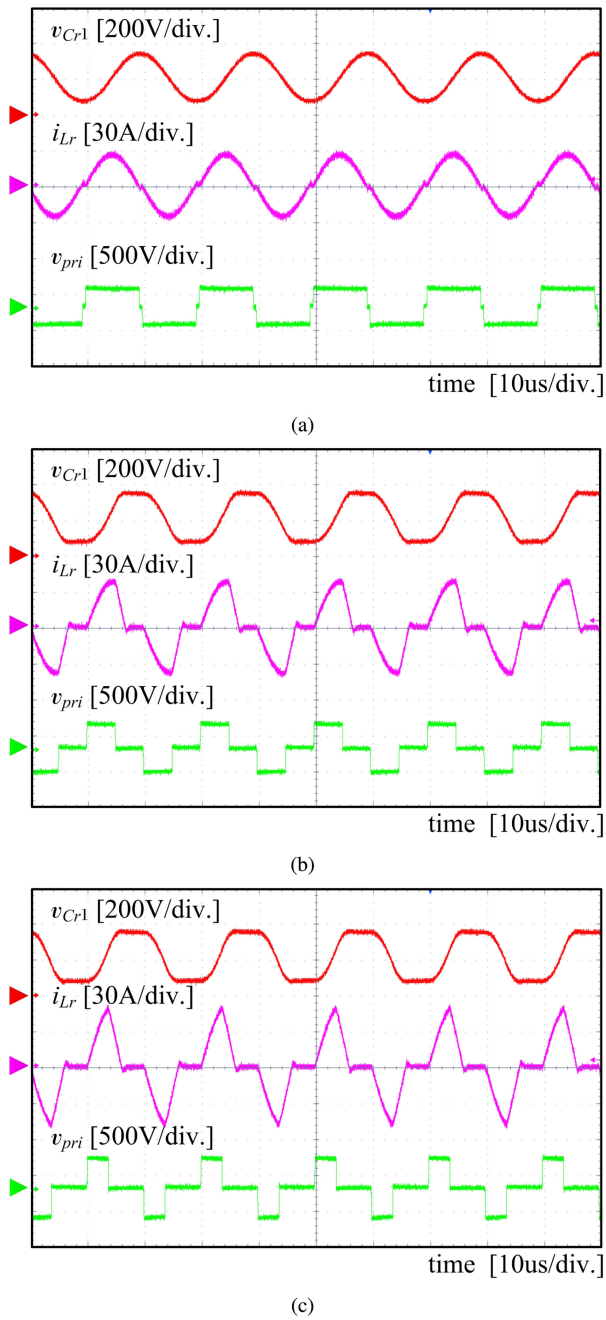

Fig. 12. Experimental waveforms of the proposed converter under full load when it operates as a full-bridge series-resonant converter. (a) $V_p = 250$ V. (b) $V_p = 330$ V. (c) $V_p = 415$ V.

For higher rated power P_s, L_r needs to be lower. But, considering the peak current stress, L_r value should be as large as possible with satisfying (44).

V. Experimental Results

To evaluate the performance of the proposed converter, we conducted experimental tests using an in-house built 3.3-kW converter prototype. We selected primary source voltage V_p from 250 to 415 V, secondary source voltage $V_s = 400$ V, and minimized the transformer turns-ratio. The general circuit component values and specific components are listed in Table I. PWM duty control functions are implemented on a TMS320F28377D digital signal processor.

In the forward direction, the converter operates as a PWM full-bridge series-resonant converter (see Figs. 11 and 12). As S_4 gets turned on, the current begins to flow through L_r following the sinusoidal curve. When S_4 gets turned off and S_3 gets turned

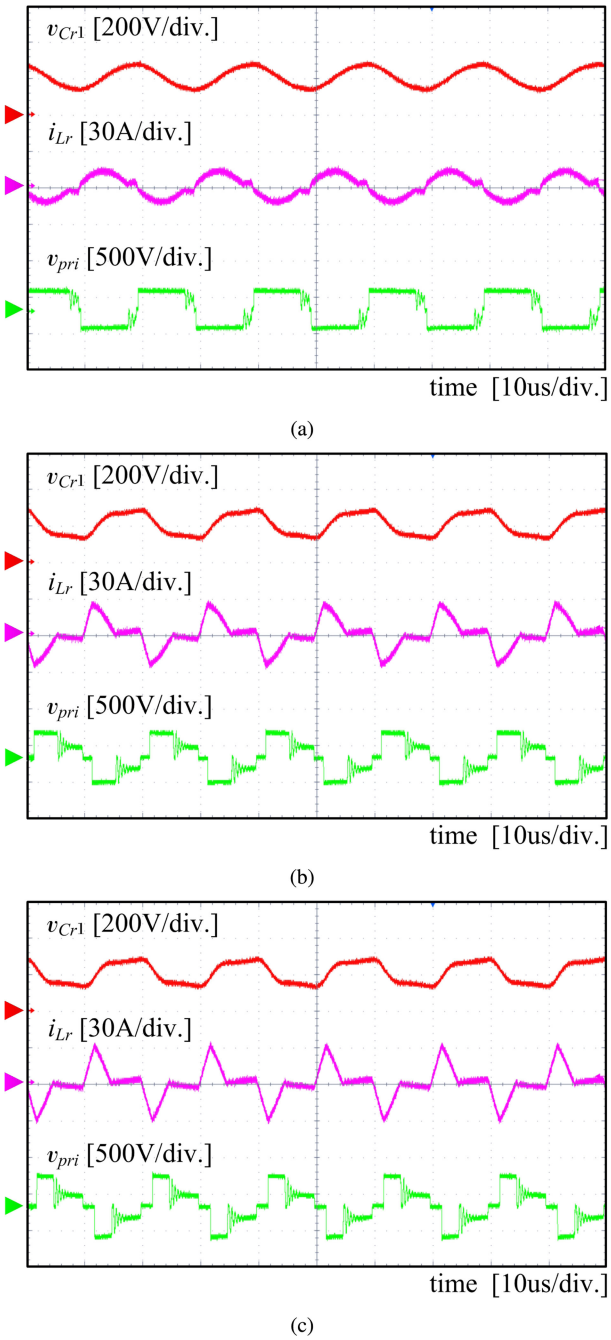

Fig. 13. Experimental waveforms of the proposed converter under half load when it operates as a half-bridge resonant boost converter. (a) $V_p = 250$ V. (b) $V_p = 330$ V. (c) $V_p = 415$ V.

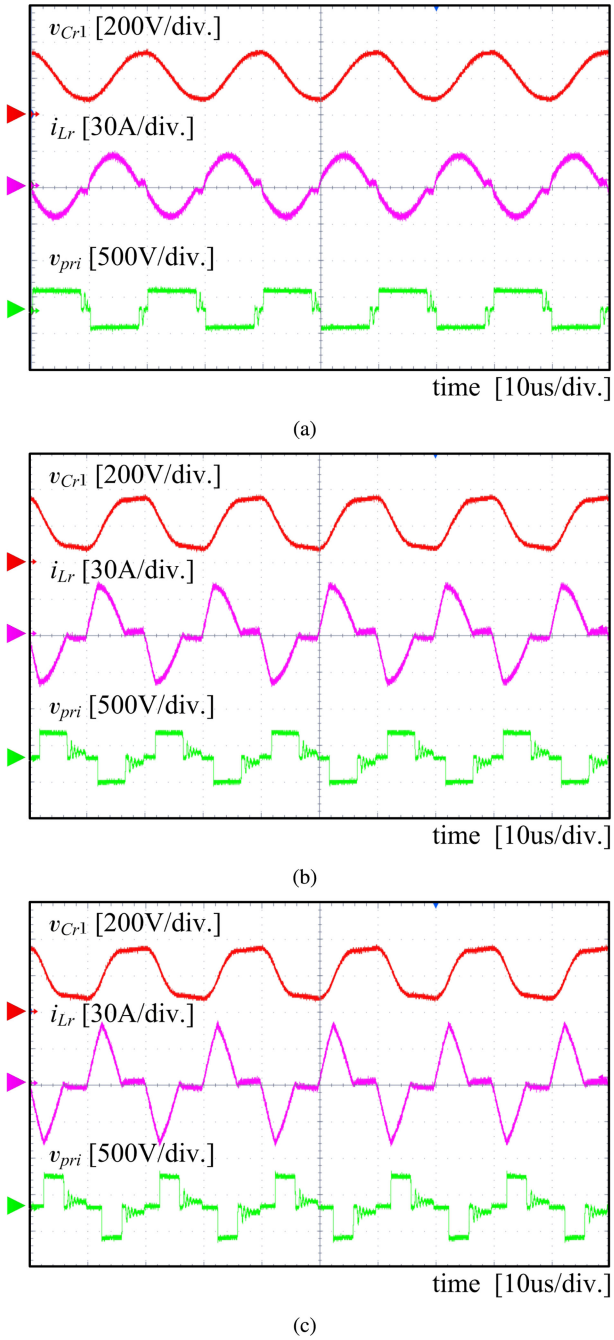

Fig. 14. Experimental waveforms of the proposed converter under full load when it operates as a half-bridge resonant boost converter. (a) $V_p = 250$ V. (b) $V_p = 330$ V. (c) $V_p = 415$ V.

on, i_{Lr} quickly goes to 0. In the backward direction, the converter operates as a half-bridge resonant boost converter (see Figs. 13 and 14). As S_6 gets turned on, the resonant inductor current increases quickly following the uphill part of the sinusoidal curve. When S_4 gets turned off, the resonant inductor current decreases following the downhill part of the sinusoidal curve. We also verified ZVS operation of the switches under 30% load with $V_p = 250$, 330, and 415 V in forward direction (see Fig. 15) and under full load with $V_p = 250$, 330, and 415 V in backward direction (see Fig. 16). Achieving ZVS is harder with lighter load in forward operation and with heavier load in backward operation, as shown in Fig. 10. In theoretical analysis, complete ZVS operation occurs at 30% load and 0.6 voltage gain (with $V_p = 415$ V) in forward direction [see Fig. 10(a)]; ZVS can be achieved under full load in backward direction [see Fig. 10(b)]. In the experiments, complete ZVS operation also occurs at 30% load and $V_p = 415$ V [see Fig. 15(c)]; ZVS can also be achieved under full load in backward direction [see Fig. 16(c)].

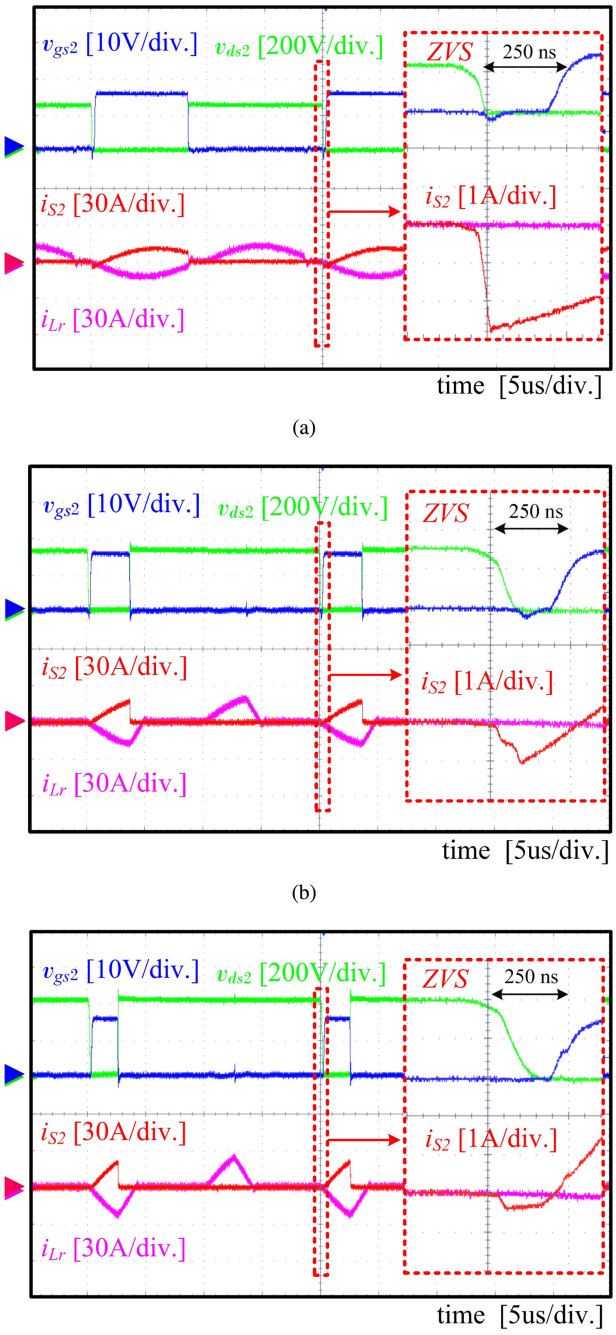

Fig. 15. Experimental waveforms of gate–source voltage, drain–source voltage, switch current, and resonant current with $V_s = 400$ V at 30% load in forward direction. (a) S_2 with $V_p = 250$ V. (b) S_2 with $V_p = 330$ V. (c) S_2 with $V_p = 415$ V.

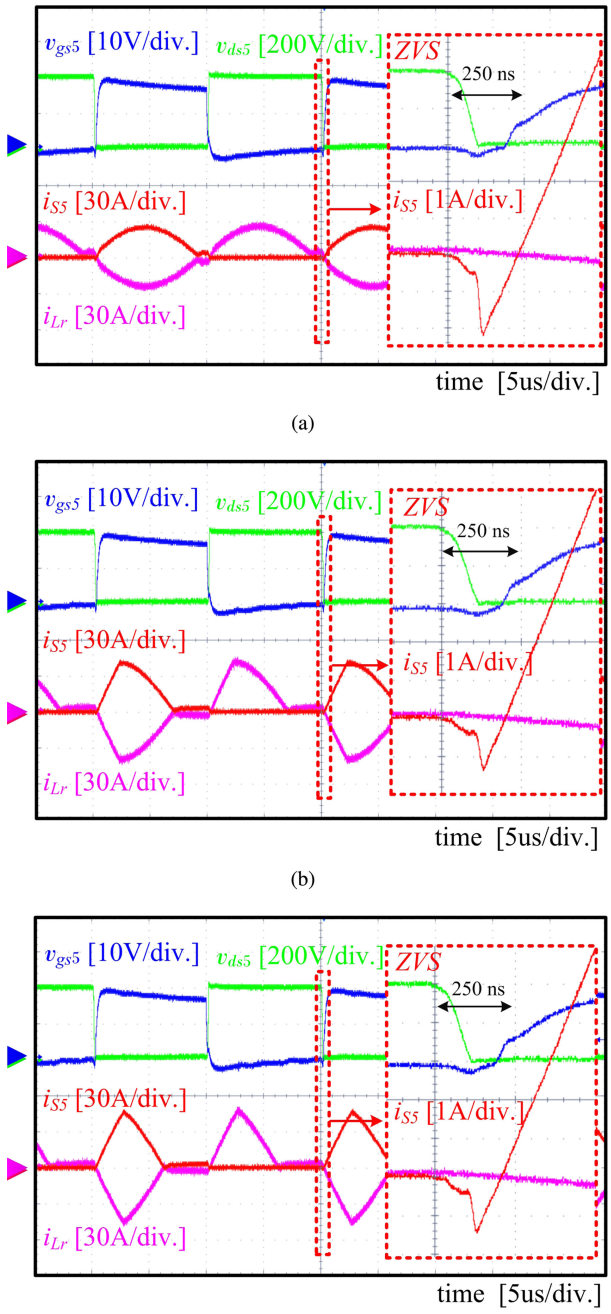

Fig. 16. Experimental waveforms of gate–source voltage, drain–source voltage, switch current, and resonant current with $V_s = 400$ V at full load in backward direction. (a) S_5 with $V_p = 250$ V. (b) S_5 with $V_p = 330$ V. (c) S_5 with $V_p = 415$ V.

In order to show the dynamic performance of the proposed converter, we varied the reference output power from 1 kW to 500 W and vice versa in both power flow directions (see Fig. 17). The primary current well tracks the reference primary current under the reference output power variation. We also tested the performance of the proposed converter when the power flow direction changes (see Fig. 18). Similar tendency is observed under the transition of the power flow direction.

The power conversion efficiency was measured by Yokogawa WT330 digital power meter (Fig. 19). The maximum measured efficiency is 97.8% in the forward direction and 97.8% in the backward direction. The California Energy Commission efficiency is 97.5% in the forward direction and 97.4% in the backward direction at $V_p = 250$ V. Fig. 20 shows the power loss distribution of the proposed converter at full-load. In Fig. 20(a), the primary switch loss takes 41.58% and the secondary switch

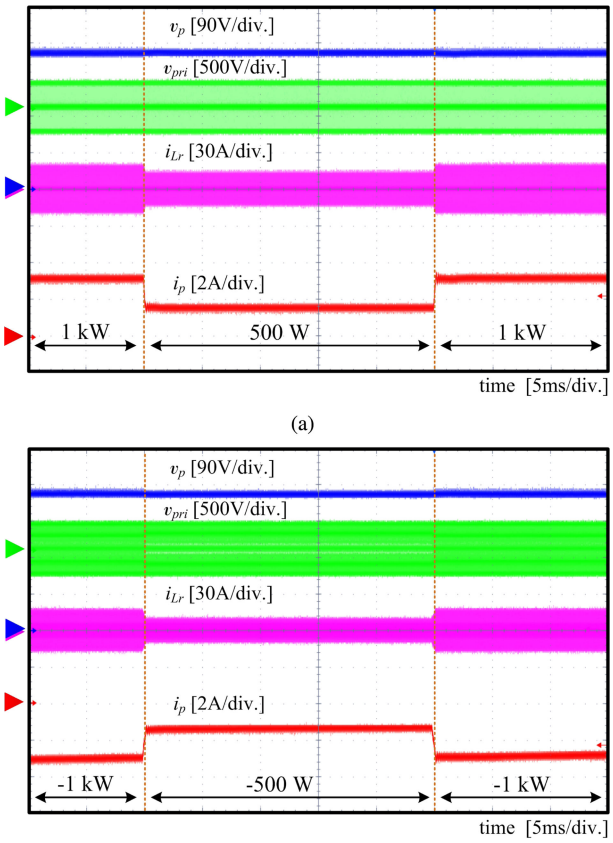

Fig. 17. Experimental waveforms of the proposed converter when load step change occurs at $V_p = 330$ V and $V_s = 400$ V. (a) Forward direction. (b) Backward direction.

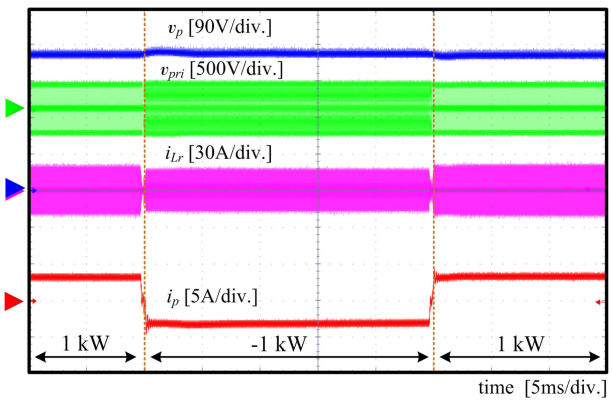

Fig. 18. Experimental waveforms of the proposed converter when power flow direction changes at $V_p = 330$ V and $V_s = 400$ V.

loss takes 19.08% in total power loss in the forward direction. In Fig. 20(b), the primary switch loss takes 39.58% and the secondary switch loss takes 22.54% in total power loss in the backward direction.

VI. Discussions

Different converters are compared according to the operation modes, the number of components, efficiency, etc. (Table II).

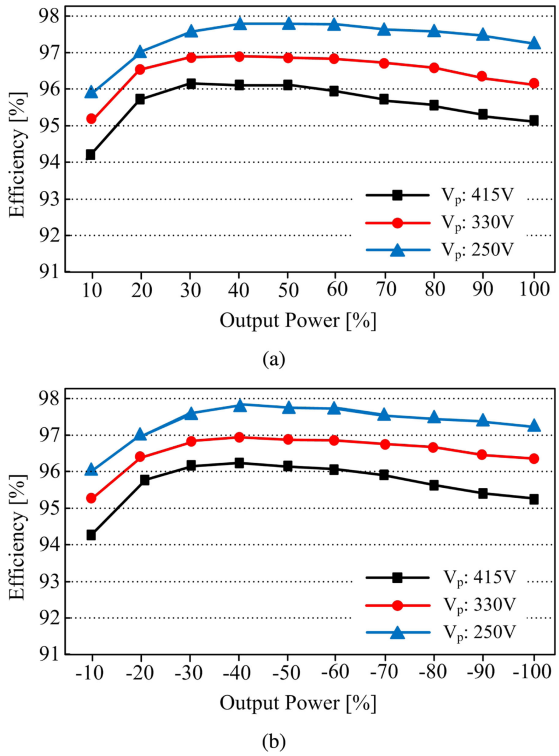

Fig. 19. Measured efficiency curves of the proposed converter for various range of battery voltages according to the output power. (a) Forward operation. (b) Backward operation.

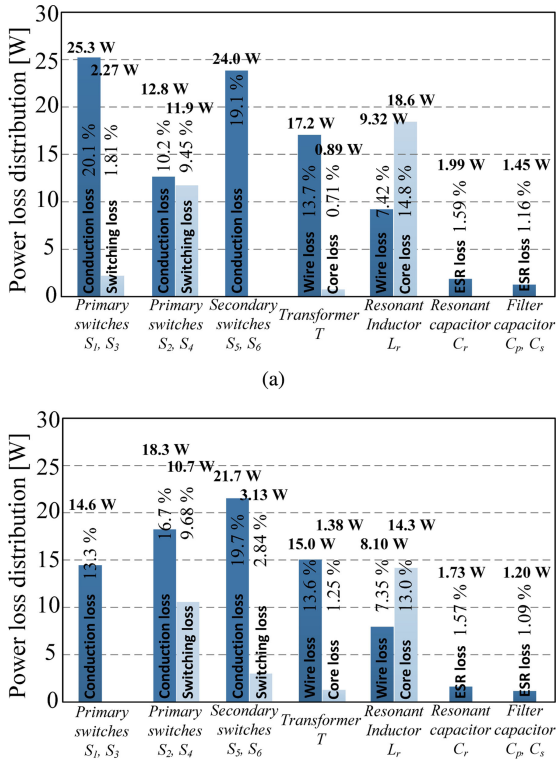

Fig. 20. Power loss distribution of the proposed converter at $V_p = 330$ V and $V_s = 400$ V under the full-load. (a) Forward direction. (b) Backward direction.

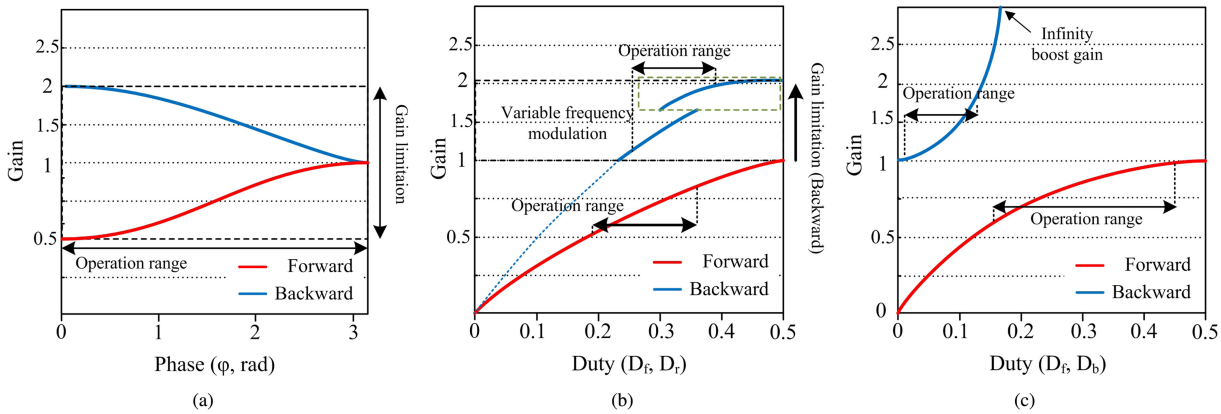

Fig. 21. Voltage gains of bidirectional resonant converters. (a) Converter in [15]. (b) Converter in [16]. (c) Proposed converter.

TABLE II
COMPARISON OF CONVENTIONAL CONVERTERS AND PROPOSED CONVERTER

Configurations		[1–4]	[14]	[15]	[16]	Proposed converter
Topology		DAB	PWAM 3-Level LLC	Half bridge + Full bridge & Half bridge	Full bridge + Full bridge	Full bridge + Active voltage -doubler
Converter operation	Forward	Buck-Boost	Buck-Boost	Buck-Boost	Buck	Buck
	Backward	Buck-Boost	Buck-Boost	Buck-Boost	Buck	Boost
Inductor current	Forward	Linear	Resonant	Resonant	Resonant	Resonant
	Backward	Linear	Resonant	Resonant	Resonant	Resonant
Frequency variation		Fixed	Fixed	Fixed	Fixed+Variable	Fixed
Switches		8	12	8	8	6
Passive Components		1	2	3	2	3
Voltage gain range	Forward mode	$0-\infty$	$0-1$	$0.5-1$	$0-1$	$0-1$
	Backward mode	$0-\infty$	$1-\infty$	$1-2$	$1-2$	$1-\infty$
Peak efficiency	Forward	97.0 %	96.5 %	98.3 %	97.7 %	97.8 %
	Backward	≈97.0 %	≈96.5 %	98.2 %	97.3 %	97.8 %
Rated power		1 kW	1 kW	1 kW	6.6 kW	3.3 kW
Cost		Low	High	Medium	Medium	Low
Modulation		Medium	Complex	Medium	Medium	Simple

The DAB converter [1]–[4] suffers from high reactive power and high turn-OFF loss when the battery voltage deviates from the nominal one. The PWAM three-level *LLC* converter [14] can suppress the switching frequency variation over wide range of battery voltages, but it requires a large number of components. Shen *et al.* [15] proposes a hybrid mode bidirectional resonant converter that operates in a full-bridge mode and a half-bridge mode in both bidirectional power flow to achieve 0.5-to-1 voltage gain. By using different circuits for different modes, Lee *et al.* [16] was able to double the voltage gain. However, both converters must increase the switching frequency when the battery voltage is very low. Compared to [15] and [16], the proposed converter achieves higher voltage conversion ratio by operating it as a PWM full-bridge series-resonant converter in the forward direction and a half-bridge resonant boost converter in the backward direction. Thus, the switching frequency is not required to change. We compared forward/backward voltage gain ranges of the converters in [15] and [16] and the proposed converter (see Fig. 21). It also requires only six switches so that the hardware implementation cost of the proposed converter becomes much lower than the converters in [15], [16].

The same topology appeared in [18], but the operational characteristics is quite different. In [18], the circuit operates mainly for unidirectional power transfer. When the input voltage is higher than the nominal one, the converter operates in a phase-shift full-bridge series-resonant converter (PSFB-SRC) mode. When the input voltage is lower than the nominal one, the converter operates in the resonant-boost mode. On the contrary, the proposed converter operates for bidirectional power transfer. In the forward direction, the proposed converter is able to operate as a PSFB-SRC but the hard-switching turn-OFF occurs in the leading-leg switches. To minimize turn-OFF loss, an additional SiC MOSFET needs to be used for S_1, which increases the development cost. Thus, we operate the proposed converter as a PWM full-bridge series-resonant converter in the forward direction, in which hard-switching turn-OFF occurs only at

the bottom switches as in the half-bridge resonant boost converter in the backward direction. Furthermore, the converter operating in the resonant boost mode [18] cannot achieve ZVS turn-ON in the secondary switches due to the voltage doubler structure on the secondary side. But the proposed converter is able to turn ON the bottom switches with ZVS in the backward mode operation by taking advantage of the bridgeless structure.

VII. Conclusion

This article presents a highly efficient bidirectional series-resonant dc/dc converter over wide range of battery voltages for V2G-capable EVs. The proposed converter is equipped with a full-bridge circuit on the primary side and an active voltage doubler circuit on the secondary side. Using only six active switches, we can reduce the size and cost of the proposed converter. Two SiC MOSFETs are used on the bottom switches of the primary side to reduce high turn-OFF loss. By operating the circuit as a PWM full-bridge series-resonant converter during the forward mode operation and a half-bridge resonant boost converter during the backward mode operation, the proposed converter achieves high efficiency over wide range of battery voltages. This circuit also operates with fixed frequency and with PWM control, and thus, the optimized magnetic components and filters can be designed dedicated to that frequency. To confirm the validity of the proposed converter, a 3.3-kW prototype converter was built and tested. Under the designated power and battery voltage ranges, it achieved 97.8% peak efficiency in both forward and backward directions.

Acknowledgements

The authors would like to thank Dr. J. S. Lee for his assistance with this article.

References

[1] B. Zhao, Q. Song, W. Liu, G. Liu, and Y. Zhao, "Universal high-frequency-link characterization and practical fundamental-optimal strategy for dual-active-bridge DC-DC converter under PWM plus phase-shift control," *IEEE Trans. Power Electron.*, vol. 30, no. 12, pp. 6488–6494, Dec. 2015.

[2] Y. W. Cho, W. J. Cha, J. M. Kwon, and B. H. Kwon, "High-efficiency bidirectional DAB inverter using a novel hybrid modulation for stand-alone power generating system with low input voltage," *IEEE Trans. Power Electron*, vol. 31, no. 6, pp. 4138–4147, Jun. 2016.

[3] A. Tong, L. Hang, and S. Gao, "Modeling and analysis of dual-active-bridge isolated bidirectional DC/DC converter to minimize RMS current with whole operating range," *IEEE Trans. Power Electron.*, vol. 33, no. 6, pp. 5302–5316, Jun. 2017.

[4] B. Han, C. K. Bae, J. S. Lee, and M. Kim, "Repetitive controller of capacitor-less current-fed dual-half-bridge converter for grid-connected fuel-cell system," *IEEE Trans. Ind. Electron.*, vol. 65, no. 10, pp. 7841–7855, Oct. 2018.

[5] B. Zhao, Q. Yu, and W. Sun, "Extended-phase-shift control of isolated bidirectional DC–DC converter for power distribution in microgrid," *IEEE Trans. Power Electron.*, vol. 27, no. 11, pp. 4667–4680, Nov. 2012.

[6] X. Liu *et al.*, "Novel dual-phase-shift control with bidirectional inner phase shifts for a dual-active-bridge converter having low surge current and stable power control," *IEEE Trans. Power Electron.*, vol. 32, no. 5, pp. 4095–4106, May 2017.

[7] S. S. Muthuraj, V. K. Kanakesh, P. Das, and S. K. Panda, "Triple phase shift control of an LLL tank based bidirectional dual active bridge converter," *IEEE Trans. Power Electron.*, vol. 32, no. 10, pp. 8035–8053, Oct. 2017.

[8] F. Musavi, M. Craciun, D. S. Gautam, W. Eberle, and W. G. Dunford, "An LLC resonant DC–DC converter for wide output voltage range battery charging applications," *IEEE Trans. Power Electron.*, vol. 28, no. 12, pp. 5437–5445, Dec. 2013.

[9] F. Musavi, M. Craciun, D. S. Gautam, and W. Eberle, "Control strategies for wide output voltage range LLC resonant DC–DC converters in battery chargers," *IEEE Trans. Veh. Technol.*, vol. 63, no. 3, pp. 1117–1125, Mar. 2014.

[10] J. H. Jung, H. S. Kim, M. H. Ryu, and J. W. Baek, "Design methodology of bidirectional CLLC resonant converter for high-frequency isolation of DC distribution systems," *IEEE Trans. Power Electron.*, vol. 28, no. 4, pp. 1741–1755, Apr. 2013.

[11] Z. U. Zahid, Z. M. Dalala, R. Chen, B. Chen, and J. S. Lai, "Design of bidirectional DC–DC resonant converter for vehicle-to-grid (V2G) applications," *IEEE Trans. Transport. Electrific.*, vol. 1, no. 3, pp. 232–244, Oct. 2015.

[12] S. Zou, J. Lu, A. Mallik, and A. Khaligh, "Bi-directional CLLC converter with synchronous rectification for plug-in electric vehicles," *IEEE Trans. Ind. Appl.*, vol. 54, no. 2, pp. 998–1005, Mar./Apr. 2017.

[13] A. Mallik and A. Khaligh, "Maximum efficiency tracking of an integrated two-staged AC-DC converter using variable DC link voltage," *IEEE Trans. Ind. Electron.*, vol. 65, no. 11, pp. 8409–8421, Nov. 2018.

[14] T. Jiang, J. Zhang, X. Wu, K. Sheng, and Y. Wang, "A bidirectional three-level LLC resonant converter with PWAM control," *IEEE Trans. Power Electron.*, vol. 31, no. 3, pp. 2213–2225, Mar. 2016.

[15] Y. Shen, H. Wang, A. Al-Durra, Z. Qin, and F. Blaabjerg, "A bidirectional resonant DC–DC converter suitable for wide voltage gain range," *IEEE Trans. Power Electron.*, vol. 33, no. 4, pp. 2957–2975, Apr. 2018.

[16] B. K. Lee, J. P. Kim, S. G. Kim, and J. Y. Lee, "An isolated/bidirectional PWM resonant converter for V2G (H) EV on-board charger," *IEEE Trans. Veh. Technol.*, vol. 66, no. 9, pp. 7741–7750, Sep. 2017.

[17] Y. Shen, H. Wang, Z. Shen, Y. Yang, and F. Blaabjerg, "A 1-MHz series resonant dc-dc converter with a dual-mode rectifier for PV microinverters," *IEEE Trans. Power Electron.*, vol. 34, no. 7, pp. 6544–6564, Jul. 2019.

[18] S. Kim, B. Kim, B. H. Kwon, and M. Kim, "An active voltage-doubler rectifier based hybrid resonant DC/DC converter for wide-input-range thermo-electric power generation," *IEEE Trans. Power Electron.*, vol. 33, no. 11, pp. 9470–9481, Nov. 2018.

Changkyu Bai (S'17) was born in Seoul, South Korea, in 1993. He received the B.S. degree in electrical engineering from the Pohang University of Science and Technology (POSTECH), Pohang, South Korea, in 2016. He is currently working toward the Ph.D. degree in creative IT engineering (CiTE) at POSTECH.

His research interests include power conversion systems and control, grid-connected inverters, and bidirectional converters.

Byeongcheol Han (S'15–M'18) was born in Busan, South Korea, in 1986. He received the B.S. degree in electrical engineering from Pusan National University, Busan, South Korea, in 2012, and the Ph.D. degree in creative IT engineering (CiTE) from the Pohang University of Science and Technology (POSTECH), Pohang, South Korea, in 2018.

In 2018, he was a Postdoctoral Researcher in CiTE with POSTECH. Since 2018, he has been a Postdoctoral Associate with the Future Energy Electronics Center, Virginia Tech, Blacksburg, VA, USA. His research interests include nonlinear systems and control, grid-connected inverters, energy storage systems, and controller design for power conversion systems.

Bong-Hwan Kwon (M'91) was born in Pohang, South Korea, in 1958. He received the B.S. degree from Kyungpook National University, Daegu, South Korea, in 1982, and the M.S. and Ph.D. degrees from the Korea Advanced Institute of Science and Technology, Seoul, South Korea, in 1984 and 1987, respectively, all in electrical engineering.

Since 1987, he has been with the Department of Electronic and Electrical Engineering, the Pohang University of Science and Technology (POSTECH), Pohang, South Korea, where he is currently a Professor. His research interests include converters for renewable energy, high-frequency converters, and switch-mode power supplies.

Minsung Kim (M'14) was born in Ulsan, South Korea, in 1986. He received the B.S. degree in electrical engineering from the Pohang University of Science and Technology (POSTECH), Pohang, South Korea, in 2008, and the Ph.D. degree in electrical engineering from POSTECH, in 2013.

Since 2013, he has been with the Department of Creative IT Engineering and Future IT Research Laboratory, POSTECH, where he was a Research Assistant Professor. In 2016, he was a Research Scholar with the Future Energy Electronics Center, Virginia Tech, Blacksburg, VA, USA. In 2017 and 2018, he has also served as an Academic Visitor at Control and Power System Group, Imperial College London, London, U.K. Since 2018, he has been with the Division of Electronics and Electrical Engineering, Dongguk University, Seoul, South Korea, where he is currently an Assistant Professor. His current research interests include highly efficient power conversion circuit design, intelligent controller design for industrial electronics, and renewable energy and energy storage systems.